A Simple Method for Estimating Horizontal Diffusivity

ANNA OLIVÉ ABELLÓ,[a] JOSEP L. PELEGRÍ,[a] AND FRANCISCO MACHÍN[b]

[a] *Departament d'Oceanografia Física i Tecnològica, Institut de Ciències del Mar, CSIC, Unidad Asociada ULPGC-CSIC, Barcelona, Spain*

[b] *Departamento de Física, Universidad de Las Palmas de Gran Canaria, Las Palmas de Gran Canaria, Spain*

(Manuscript received 20 August 2022, in final form 26 February 2023, accepted 31 March 2023)

ABSTRACT: A common dilemma for oceanographers is the choice of horizontal diffusivity. There is no single answer as we could argue that diffusion depends precisely on those processes that cannot be sampled or modeled. Here we propose the radial offset by diffusion (ROD) method as a simple model-dependent approach for estimating these coefficients, and show its application for the southwestern South Atlantic. The method compares actual displacements of field drifters with numerical trajectory predictions. The observed–predicted differences in radial positions (radial offsets), which respond to diffusive motions not captured by the numerical model, are reproduced with a one-dimensional radial-diffusive solution through a proper selection of the diffusion coefficient. The method is tested at eight depths, from the sea surface down to 2000 m, using several drifter datasets and the Parcels software applied to the GLORYS12v1 (1/12° daily) velocity outputs. In all cases the radial offsets show Gaussian distributions that are well reproduced by the radial diffusive solution. Maximum diffusivities of 4630–4980 $m^2\ s^{-1}$ happen in the upper 200 m of the water column and minimum values of 1080–1270 $m^2\ s^{-1}$ occur between 1400 and 2000 m. The 15-m diffusivity is fairly constant in latitude (3850–5270 $m^2\ s^{-1}$), but the 1000-m diffusivity decreases from 1640 to 1820 $m^2\ s^{-1}$ north of the Polar Front to 530 $m^2\ s^{-1}$ south of the Southern Boundary. A comparison with other diffusivity studies validates the good adequacy of the ROD method for numerical and field applications.

KEYWORDS: South Atlantic Ocean; Southern Ocean; Diffusion; Trajectories; Numerical analysis/modeling; Subgrid-scale processes

1. Introduction

Diffusion is a fundamental characteristic of geophysical flows, yet its description and quantification remains elusive. Diffusion indeed depends on the spatiotemporal intermittence and often associated turbulence of many processes acting at multiple scales, which are responsible for dispersing properties, so we may truly say that diffusion is process dependent. Paradoxically, if we can sample or model a certain process then we do not worry about diffusion, it naturally disappears and turns into advection. But the reality is that we are not capable of sampling or simulating all processes, there are many motions that we cannot model and become therefore enclosed under the wavy concept of turbulent diffusion.

The process dependency of diffusion is reflected in the horizontal evolution of a patch of passive tracer through three different phases, as proposed by Garrett (1983) and Sundermeyer and Price (1998). At short subinertial time scales, small-scale processes such as internal waves and other subinertial motions dominate mixing, with local (small-scale) diffusivity coefficients of order 0.1–1 $m^2\ s^{-1}$. The slowly growing patch eventually becomes large enough to be effectively stretched by straining submesoscale motions, causing long and narrow streaks. These streaks finally turn larger than the mesoscale structures and extend around each other causing much faster homogenization, reaching (effective) diffusivity coefficients on the order of 1000–10 000 $m^2\ s^{-1}$.

Biogeochemical or physical anomalies can certainly be locally introduced into the ocean, but very often, as shown by satellite images, they appear as large regional patches. This is the case when we deal with large-scale or global circulation. Either because of large-scale atmospheric forcing or as a result of the long residence times of water masses, for many regions and applications we can skip the small-scale and straining phases and turn directly to the mesoscalar high-diffusivity phase. From a practical perspective, this is also necessarily true because our large scale or global circulation models still have relatively coarse resolution (nowadays operational at 1/12° although likely improving to 1/36° in the coming years) that does not resolve most submesoscalar or small-scale motions. Hence, if we wish to hindcast or forecast the temporal evolution of large-scale processes, such as the global overturning circulation, we must resort to expressing these unresolved spatiotemporal scales in terms of effective vertical and horizontal diffusivities.

Different Lagrangian and Eulerian methods have been used to estimate the horizontal diffusion coefficients, a brief summary follows. Lagrangian diffusivity studies gained momentum during the last decades thanks to the increased availability of drifter data. Most of these works rely on statistical techniques studying the motion of single particles or the relative dispersion of groups of particles (Davis 1987, 1991a,b; Babiano et al. 1990; Zhurbas and Oh 2003; LaCasce 2008; Chiswell 2013; LaCasce et al. 2014; Zhurbas et al. 2014; Balwada et al. 2021), although other studies have assessed the rate of material transport across

Supplemental information related to this paper is available at the Journals Online website: https://doi.org/10.1175/JTECH-D-22-0097.s1.

Corresponding authors: Anna Olivé Abelló, aolive@icm.csic.es; Josep L. Pelegrí, pelegri@icm.csic.es

DOI: 10.1175/JTECH-D-22-0097.1

tracer contours (Nakamura 1996; Abernathey and Marshall 2013) or have searched for diffusivities that bring the progress of numerical particles closest to the observed evolution of drifters (Döös et al. 2011; De Dominicis et al. 2012; Rühs et al. 2018).

Eulerian diffusion studies have exploited the increasing amount of hydrographic data, particularly from Argo floats and altimetry data, obtaining estimates of velocity and length scales from the variance of properties and directly applying mixing length theory (Naveira Garabato et al. 2011; Abernathey and Marshall 2013; Roach et al. 2016; Roach et al. 2018). Other approaches have related eddy diffusivity with eddy kinetic energy (Naveira Garabato et al. 2011; Roach et al. 2018) or have obtained the diffusion coefficients by adjusting the distribution of properties through inverse methods (Zika et al. 2010; Cole et al. 2015; Deng et al. 2014). Remarkably, the mapping of the temporal evolution of artificial or natural tracers, as observed in major field experiments, has also provided direct estimates of the eddy diffusion coefficients (Ledwell et al. 1998; Sundermeyer and Price 1998; Naveira-Garabato et al. 2007; Tulloch et al. 2014; Boland et al. 2015).

The horizontal diffusivity values that have arisen from all the above studies are extremely diverse, possibly not only reflecting spatial variability in fluid dynamics but also differences in the diffusive processes under consideration. For modeling purposes, turbulent diffusion depends on the spatiotemporal scales of the model, as these define the size and temporal memory of fluctuations around the mean advective values. A general rule of the thumb is that the lower the spatiotemporal resolution of the model the larger the diffusion coefficients.

Hence, an alternative strategy could be to develop fit-to-model methods that allow obtaining the horizontal diffusion coefficients, methods simple enough to be used as an easy initial step for choosing the most appropriate coefficients for each particular application. Nowadays, the combination of the much improved operational numerical hindcasts, particularly thanks to the data assimilation of the last generation models and the growing amount of accurate drifting data, opens the possibility of a simple Lagrangian approximation to obtain model-fit diffusion coefficients. Here we propose the radial offset by diffusion (ROD) method as a simple tool that calculates the difference in radial position between float and equivalent numerical trajectories, whose Gaussian distribution is then adjusted with a simple radial diffusive model.

We first introduce the Subantarctic Atlantic case-study area and the field and numerical data to be used for our tests (section 2), and next describe the fundamentals of the ROD method (section 3). We then apply the method to the entire study area at eight different depths and explore the spatial variability near the sea surface and at 1000-m depth for five regions, which are separated by the Antarctic and Subantarctic frontal systems (section 4). In section 5 we discuss the limitations and advantages of the method, and compare our results with other observations for the case-study area. We end with some final thoughts in section 6.

2. Data

a. Case-study area

With the objective of testing the method, we have used field and numerical data from the Drake Passage (64°W) to 10°W and between 36° and 64°S (Fig. 1). The case-study area is the southwestern South Atlantic and the corresponding sector of the Southern Ocean, including the Scotia Sea, covering the whole range of circumpolar, Antarctic, and Subantarctic Waters. The dynamics of the area are largely controlled by the Southern Ocean frontal systems: Subantarctic Front (SAF), Polar Front (PF), Southern Antarctic Circumpolar Current Front (SACCF), and the Southern Boundary (SB) (Olivé Abelló et al. 2021) (Fig. 1d). These frontal systems cross the Drake Passage and stretch first zonally into the Scotia Sea and then northward and northeastward through the North Scotia Ridge, steering most of the circumpolar waters that enter the South Atlantic Ocean.

b. Global Drifter Program data

The Global Drifter Program (GDP) started in 1995, although the oldest data records go back to 1979. The GDP maintains a fleet of about 1300 drifters with a holey-sock-type drogue centered at 15 m. All drifters sample surface temperature, although most drifters typically incorporate other sensors such as surface pressure and salinity. The drifters originally placed themselves using the Argos positioning system (CLS 2011), with typical 100-m resolution and several fixings per day, although during recent years they have progressively switched to the global positioning system (GPS), which provides hourly data with resolution of order 1 m. The drifter database, which is available in near–real time through the GDP website (https://www.aoml.noaa.gov/phod/gdp/), consists of quality-controlled 6-hourly interpolated location, time, velocity, and temperature with a position accuracy of about 100 m (Elipot et al. 2016).

We have used the trajectories from a total of 301 drifters that crossed the Drake Passage through 64°W and traveled the study area between 2005 and 2020 (Figs. 1c,e). For our purposes, the 6-h positions are used to generate consecutive cycles of 10-day displacements (Figs. 1c,f).

c. RAFOS floats

The RAFOS floats are neutrally buoyant instrumented drifters that receive acoustic signals emitted by several moored sound sources and hence calculate their position via triangulation; their position is provided daily with an estimated accuracy of about 1 km (Rossby et al. 1986; Balwada et al. 2016). Here we have used a subset of 32 floats that were tracked between 2009 and 2011 as part of the Diapycnal and Isopycnal Mixing Experiment in the Southern Ocean (DIMES) (Balwada et al. 2016, 2021). These represent all floats crossing the Drake Passage through 68°W and entering the Scotia Sea (Figs. 1a,e).

The DIMES RAFOS floats drifted at varying depths, between 400 and 2200 m. Most of the floats wandered at depths between 1200 and 1600 m, although there were also a substantial number of displacements at other depths, particularly

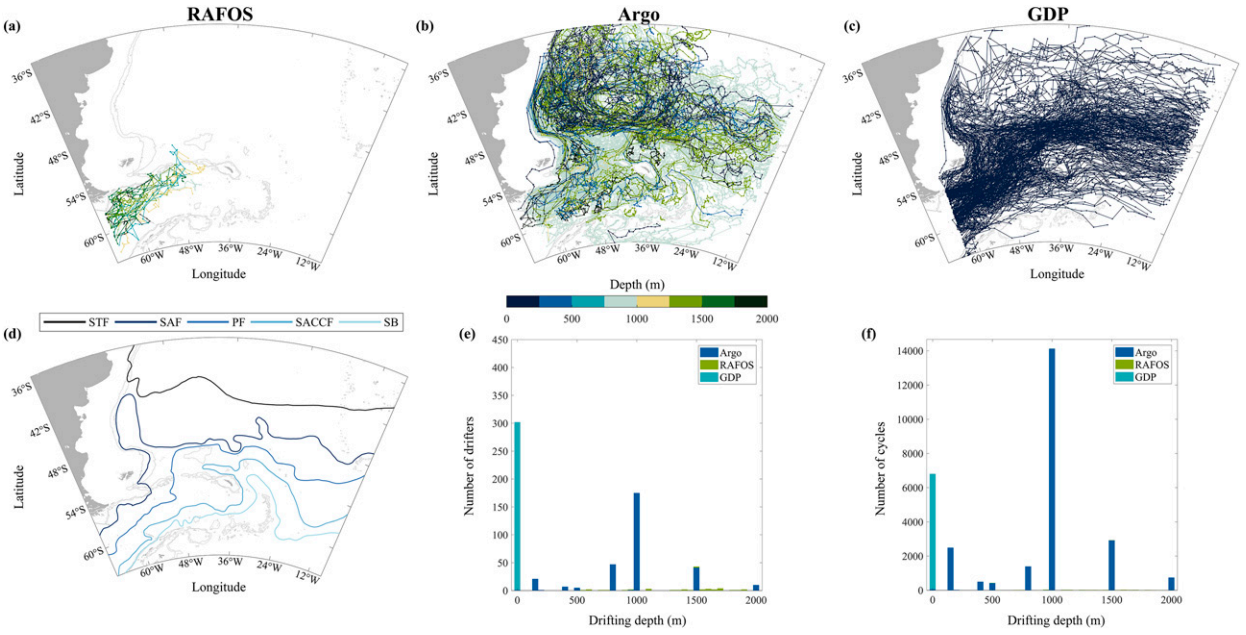

FIG. 1. Trajectories of (a) RAFOS floats between 2009 and 2011, (b) Argo floats from 2002 to 2020, and (c) GDP drifters from 2005 to 2020, with positions shown every 10 days; the RAFOS and Argo floats are colored according to their drifting depths. (d) Location of the Subtropical Front (STF), the Subantarctic Front (SAF), the Polar Front (PF), the Southern Antarctic Circumpolar Current Front (SACCF), and the Southern Boundary (SB), as obtained by Orsi et al. (1995). (e) Number of drifters and (f) number of 10-day positions according to drifting depth and the type of drifter.

between 700 and 800 m and between 1700 and 1800 m (Fig. S1 in the online supplemental material). For our purposes, the daily positions are used to produce consecutive cycles of 10-day displacements (Figs. 1a,f).

d. *Argo floats*

Since the first deployments in 1999, many Argo profiling floats have been launched worldwide as part of the International Argo Program (Argo 2000). The Argo array reached 3000 floats in 2007, and has been sustained at about 4000 for the last few years (Roemmich et al. 2022). These floats provide not only an extremely valuable sampling of the hydrographic conditions in the upper 2000 m of the water column but also offer a unique description of the flow at their parking depths (Ollitrault et al. 2006; Lebedev et al. 2007; Rosell-Fieschi et al. 2015). Every 10 days, the floats surface to transmit the collected hydrographic data, providing also an estimate of their 10-day average velocity. The 10-day displacement is calculated as a straight trajectory between the last position of the float before diving and the first position of the float as it returns to the sea surface. Rosell-Fieschi et al. (2015) estimated that the errors in the parking-depth velocities at 1000 m are less than 10% in 94% of the cases and less than 3% in 58% of the cases; for a displacement of about 50 km in 10 days this last value represents an accuracy of 1.5 km.

We have considered all Argo floats that entered the study area through the Drake Passage between 2002 and 2020 (Figs. 1b,e). The total number of floats was 310 with most of them (175) having a parking depth at 1000 m. For our analysis we have removed all float cycles when the first or last surface positions were not flagged as good (Figs. 1b,f).

e. *GLORYS12v1 reanalysis*

We use daily three-dimensional velocity fields from the global physical reanalysis GLORYS12v1 (Garric et al. 2017; Lellouche et al. 2021), developed by the Mercator Ocean team and distributed by the Copernicus Marine Environment Monitoring Service (CMEMS; http://marine.copernicus.eu), which is eddy resolving in our study area. This ocean reanalysis combines the NEMO ocean general circulation numerical model with observations to generate the best possible estimate of the state of the ocean. In particular, the GLORYS12v1 numerical data encompass the entire period of all available float and drifter observations, allowing the comparison of numerical and field trajectories (section 3a).

GLORYS12v1 has a horizontal resolution of 1/12° and 50 vertical levels. This horizontal grid means latitude–longitude cells of 7.5 km × 7.5 km at the equator and 7.5 km × 4 km at 64°S, while the vertical grid has maximum resolution at the sea surface that decreases with depth. Reanalysis products such as GLORYS12v1 are significantly accurate, in good general agreement with observations (Mignac et al. 2018; Orúe-Echevarría et al. 2021).

GLORYS12v1 includes small horizontal diffusion to avoid numerical instabilities: a standard along-isopycnal diffusivity coefficient of 100 $m^2\ s^{-1}$ is used in the Laplacian terms for tracers and momentum, plus a biharmonic diffusion coefficient with absolute value $1.25 \times 10^{10}\ m^4\ s^{-1}$ that sets the size

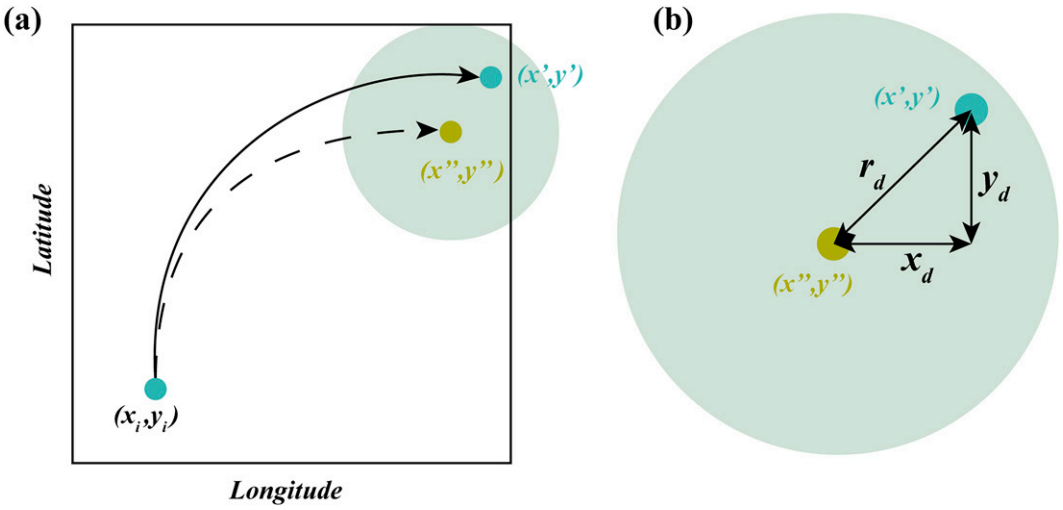

FIG. 2. (a) Schematic trajectories of a drifter and the corresponding simulated numerical particle. The initial position of both drifter and numerical particle is (x_i, y_i), and their final locations after 10 days are (x', y') and (x'', y''), respectively. (b) Sketch of the final positions of both drifter and numerical particle: the longitudinal and latitudinal offsets are $x_d = x' - x''$ and $y_d = y' - y''$, respectively, so that the offset (radial distance) is $r_d = (x_d^2 + y_d^2)^{1/2}$.

of a bi-Laplacian term in the momentum equation (Mercator Ocean 2018). This last coefficient aims at removing gridscale noise; its actual value may be understood as the fraction $\Delta x^4/\tau$, where $\Delta x = 5.7$ km is a characteristic grid size and $\tau = 1$ day is the model's time step (e.g., Gent and McWilliams 1990; Roberts and Marshall 1998). In practice, these diffusivity coefficients represent subgrid horizontal motions that are much weaker than the values obtained with the ROD method and hence, hereafter, we will assume that the model is free of diffusion.

3. Methods

a. Comparing the field and numerical positions

The numerical particles are released at the same position, depth, and day of the year as the real drifter, and tracked daily during 10 days with the advectionRK4 kernel in the open-source Parcels software (Lange and van Sebille 2017; Delandmeter and Van Sebille 2019), using the GLORYS12v1 reanalysis daily velocity fields. Setting the time interval between positions as 10 days simply responds to the characteristic surfacing cycle of the Argo floats, which represent most of our available subsurface trajectories.

Each drifter is modeled individually but for the overall numerical-field comparison (see below) the data are split into the GDP trajectories at 15 m and the float trajectories in the following seven depth ranges: 150–200, 400–500, 700–800, 900–1100, 1200–1300, 1400–1600, and 1800–2000 m. The numerical trajectories that correspond to the GDP and Argo drifters are calculated using only the horizontal velocities. However, the RAFOS floats also incorporate vertical velocities, because these drifters can display vertical motions as large as 200 m in response to the large tilting of isopycnals in frontal systems; hence, in the case of RAFOS, it may happen that data from one float split into several vertical ranges.

The numerical trajectories reflect only a small diffusivity that is added to the model for computational reasons. Hence, submesoscalar motions have to be simulated through some additional random motion proportional to a realistic subgrid horizontal diffusivity (e.g., Peña-Izquierdo et al. 2015; Vallès-Casanova et al. 2022). In contrast, the drifters do have the full spatiotemporal range of horizontal motions—except those at spatial scales smaller than the size of the drifter—so they incorporate the principal subgrid motions that are not deterministically calculated by the numerical models. Hence, by releasing numerical particles at the same time and location as the actual drifter and tracking them during a certain time interval (in our case 10 days), we can infer the motions associated with the subgrid motions.

The procedure to determine the diffusive (subgrid) motions is illustrated in Fig. 2. Let us call (x_i, y_i) the initial location of both the drifter and the numerical particle, and (x', y') and (x'', y'') the positions of the drifter and the numerical particle after 10 days, respectively. Naming $x_d = x' - x''$ and $y_d = y' - y''$ the longitudinal and latitudinal offsets, then the total offset (radial distance) is given by $r_d = (x_d^2 + y_d^2)^{1/2}$.

Figure 3 illustrates the procedure as applied to one Argo float that crossed the study area, in this particular case with a total of 53 cycles of 10 days each. We first calculate the float and numerical displacements for each cycle, leading to a scatterplot with 53 offsets (Fig. 3b). This is then repeated for all floats drifting at similar depths, for example for all RAFOS and Argo floats. These offsets are finally gathered together for the geographic area of interest; for example, the offsets for all GDP drifters (flowing at 15 m) or the offsets for the Argo and RAFOS floats that drift at 1000 m, either over the entire area of study or for some specific region (supplemental Figs. S2 and S3).

It may happen that the center of mass of the cloud of radial offsets does not coincide with the origin of coordinates for the

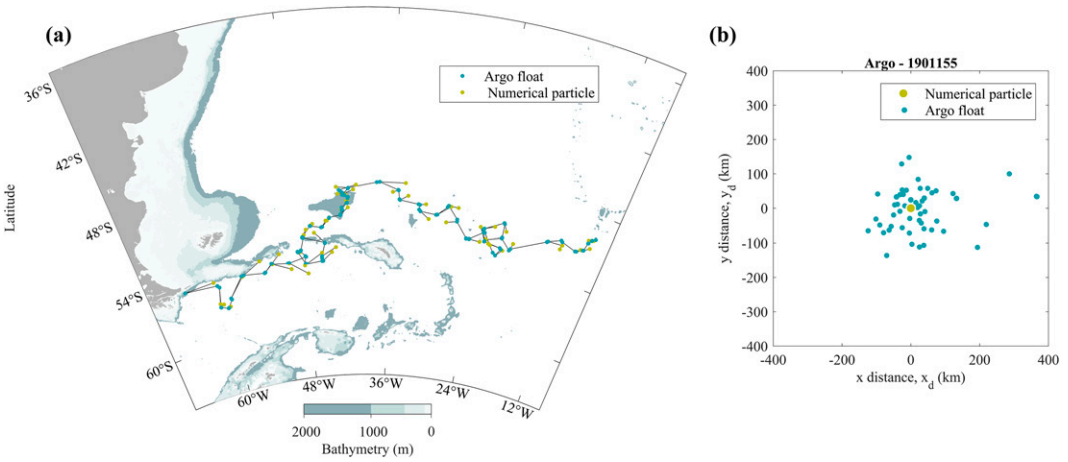

FIG. 3. (a) Sample trajectory of an Argo float through the study area, with the color convention following Fig. 2. The blue dots, joined by black lines, represent the initial and final positions transmitted by the float during the 10-day cycles; note that there are pairs of blue dots very close to each other, which represent the first transmission of the float after arrival to the sea surface and the last transmission before immersion. The numerical trajectories are drawn as black lines that depart from the second blue dot and end in a green dot, which represents the final numerical positions. (b) Scatterplot showing the radial offsets between the Argo float and the corresponding numerical particles; the origin of coordinates, which is shown as a green dot, represents the position of the numerical particle at the end of each cycle.

scatter diagram—an origin that represents the positions reached by the numerical particles—meaning that there is some bias in the mean flow as predicted by the model in comparison to what is observed by the drifter. If this is so then we simply shift the entire cloud to make the center of mass fit the origin of coordinates, recognizing that the bias is inherent to the model and not to the subgrid diffusive processes (supplemental Tables S1 and S2).

b. *Radial diffusion model*

The underlying premise of the ROD approach is that the radial distances between the drifter and numerical positions respond mainly to subgrid processes, i.e., to diffusive processes that are not considered by the numerical circulation model. With this idea in mind, we simulate the diffusive cloud (drifter minus numerical positions) through a simple one-dimensional radial diffusive equation:

$$\frac{\partial c}{\partial t} = \frac{1}{r}\frac{\partial}{\partial r}\left(Kr\frac{\partial c}{\partial r}\right) = \frac{K}{r}\frac{\partial}{\partial r}\left(r\frac{\partial c}{\partial r}\right), \tag{1}$$

where c stands for a concentration of particles (number of particles per unit area) and K is the horizontal diffusion coefficient or (effective) diffusivity; in this expression r is the radial coordinate of the diffusive motions, which corresponds to the radial offset r_d between the correlative displacements of the drifter and numerical particles. In the last equality we assume that the diffusivity is constant in space; for the numerical solution, we will further accept that K is constant in time.

The boundary conditions are $\partial c/\partial r = 0$ both at the origin $r = 0$ and for large radial values $r \to \infty$. For the initial condition, we set the concentration equal to one within a certain region close enough to the origin, $c(r \le R_n, t = 0) = 1$, and zero elsewhere, which essentially implies that there is an initial circular disk that contains all diffusive particles (in our case the drifters). In the next subsection we will explain how to normalize the actual number of drifters to reproduce this initial condition, but next we explain how to determine R_n.

The initial disk is imagined as characterizing an area where we initially place all drifters and numerical particles; once released, these particles will evolve with the environmental flow, either with (the drifters) or without (the numerical particles) subgrid motions. Hence, we want this area to be representative of the horizontal velocity field experienced by the numerical particles. With this in mind, we choose a rectangular area with longitudinal (d_{lon}) and latitudinal (d_{lat}) sides equal to the size of the grid cell, which we imagine as centered at each node of the numerical model. The disk with the equivalent area would have a radius given by $R_n = (d_{\mathrm{lon}}d_{\mathrm{lat}}/\pi)^{1/2}$. Considering the 1/12° resolution of GLORYS12v1, and choosing 50°S as a latitude representative of the entire area of study, we obtain a radius $R_n = 4.2$ km.

The diffusion equation is solved numerically using the MATLAB *pdepe* function for one-dimensional parabolic and elliptic partial differential equations (Skeel and Berzins 1990). It is solved in a domain of 420 km, with 100 elements of size $\delta r = 420$ m and the radial coordinate given by $r_i = i\delta r$. The initial condition is expressed as

$$c(r_i, t = 0) = \begin{cases} 1 & i < 10 \\ 0.5 & i = 10 \\ 0 & i > 10 \end{cases}.$$

Setting a concentration equal to one particle per square meter in a circle of radius R_n is equivalent to having initially $N = \pi R_n^2 = 5.54 \times 10^7$ particles.

Figure 4 shows the numerical solution of the radial diffusive equation at different times, using the above boundary and

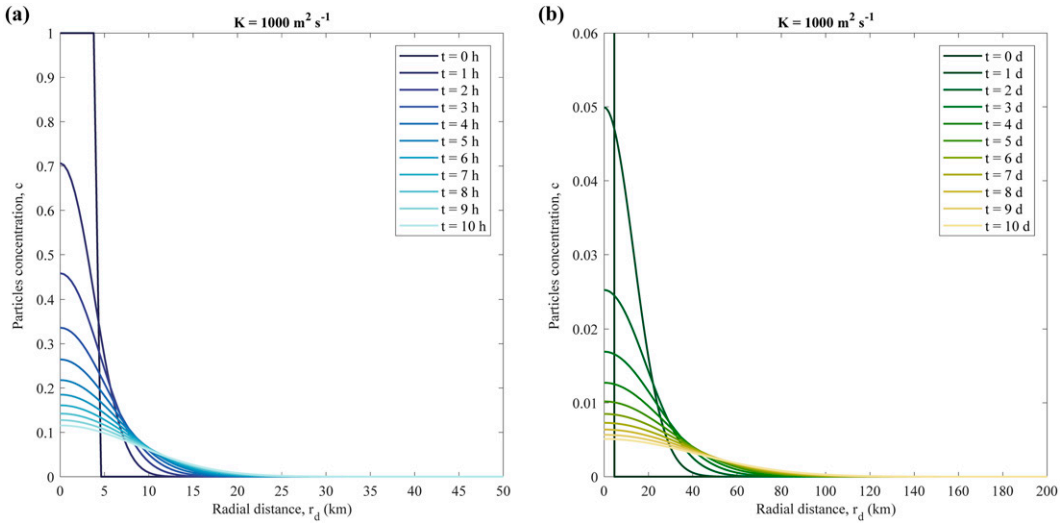

FIG. 4. Numerical solution of the radial diffusive equation for $K = 1000\ \mathrm{m^2\ s^{-1}}$ at different times. (a) From $t = 0$ to $t = 10$ h plotted every hour and (b) from $t = 0$ to $t = 10$ days plotted every day. Notice the differences in the horizontal and vertical axes between both panels.

initial conditions and a diffusion coefficient $K = 1000\ \mathrm{m^2\ s^{-1}}$. The solution at any time is Gaussian, with the concentration near the origin decreasing and the distribution flattening as particles diffuse out of their original disk. The total amount of particles (concentration integrated over the entire horizontal domain) remains constant in time, equal to the initial value N.

c. *Comparing the experimental and theoretical particle distributions*

The comparison between the radial distribution of the drifters with respect to their center of mass and the radial distribution of the concentration in the diffusion model is carried out in two steps: first, adjusting a Gaussian distribution to the drifter data, and second, selecting the diffusivity coefficient that produces the best fit between the experimental and numerical distributions.

The first step—the conversion of the cloud of radial displacements into a Gaussian distribution—requires initially producing a histogram of the number of drifters for different radial coordinates. For this purpose, the number of drifters has to be counted over equal areas, which implies that the radial coordinates of the histogram (R_j) have to be properly chosen, with the histogram radial intervals decreasing with distance from origin (Fig. 5a). Specifically, if the inner radius is R_1 then its area is going to be $A = \pi R_1^2$ and the area of any outer ring j will have to be equal to the inner area, $\pi R_j^2 - \pi R_{j-1}^2 = \pi R_1^2$, which causes that the external border of the rings increases as $R_j = j^{1/2} R_1$.

The inner radius R_1 has to be large enough to ensure that the adjacent rings gather a significant number of drifters, but it has to be small enough to provide adequate resolution near the origin. We first calculate the histograms for different values of the inner radius, starting at $R_1 = 10$ km and increasing at intervals of 10 km up to $R_1 = 80$ km, and find the Gaussian that best fits the histogram data (supplemental Fig. S4). For each case we compute the correlation between the data and the Gaussian fit, which increases with R_1 until it approximately stabilizes, and select R_1 as the minimum radius that has a high correlation value (supplemental Fig. S5). Once we have the Gaussian fit, we can interpolate the number of drifters at those same radial coordinates as for the numerical model, $r_i = i\delta r$ with $\delta r = 420$ m. Hereafter, we will use the nomenclature $R_1 = R_e$ to emphasize that it corresponds to the experimental inner radius, which differs from the inner radius R_n of the numerical model; recall that $R_n = 4.2$ km while a characteristic value of R_e is 30 km.

The second step—finding the coefficient of diffusion that produces the best agreement between the experimental and numerical distributions—requires first converting the number of drifters into an experimental concentration of particles (simply dividing by $A = \pi R_e^2$) and then normalizing this concentration by considering that the total number of numerical parcels is different to the total number of drifters. If the total number of numerical particles is $N = \pi R_n^2 = 5.54 \times 10^7$ (which sets a concentration $c = 1$ within the inner disk of radius R_n) and the total number of drifters is n (which will change depending on the depth or region considered), then the experimental concentration of particles is obtained multiplying the number of drifters by the factor N/n.

Figure 5 illustrates some of the main aspects of the previous description. A distribution of the number of particles at different radial distances (as obtained for all pairs of numerical particles and drifters) is calculated using radial intervals of equal area (Fig. 5a). The cumulative addition of the number of particles increases asymptotically until reaching the total number of observations, displaying the characteristic shape of the error function, which is the derivative of the Gaussian distribution (Fig. 5b). A Gaussian curve is finally adjusted to the normalized experimental concentrations, that is, to the number of observations per unit area after applying the N/n factor

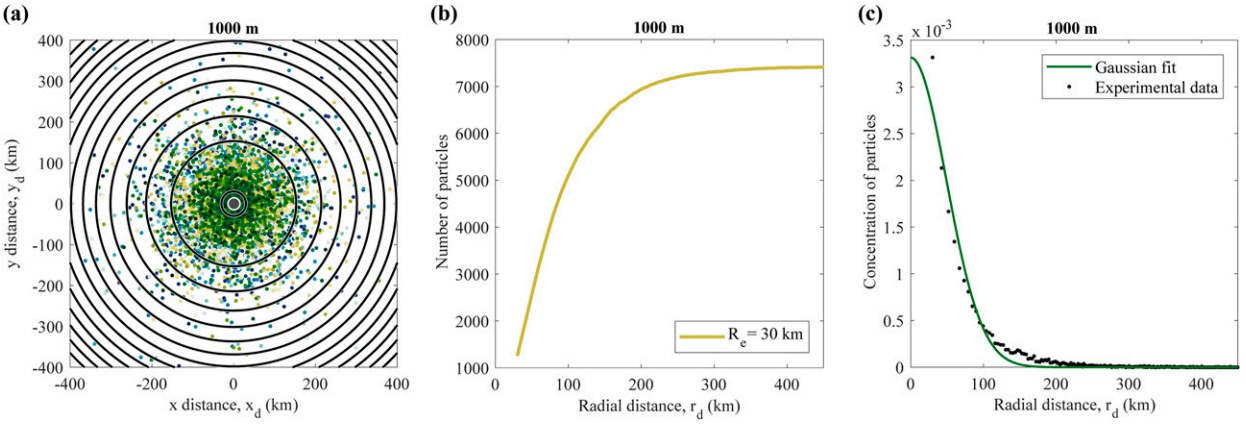

FIG. 5. (a) Scatterplot of radial offsets for drifters at 1000 m, displaying rings of equal area; the colored dots identify data points from one float. In this plot we also show the origin of coordinates (gray circle with white border) and have drawn 1 ring every 25 rings (black circles), starting with the inner ring (R_e = 30 km) and following with the relation $R_j = j^{1/2}R_e$. (b) Cumulative number of particles as a function of radial distance for R_e = 30 km, disclosing the expected shape of the error function. (c) Normalized experimental concentration (dots) and the adjusted Gaussian distribution (green line).

for proper comparison with the numerical model in section 3a (Fig. 5c).

We are finally left to comparing the values of the experimental Gaussian curve with the values of the numerical solution at t = 10 days, in both cases using the data at the radial positions $r_i = i\delta r$. For this comparison, we compute the numerical solution for different horizontal diffusive coefficients K, increasing from 0 to 10 000 m^2 s^{-1} at intervals of 10 m^2 s^{-1}. The best fit is selected as the numerical curve that produces the minimum standard deviation between both distributions, as shown in next section.

4. Results

a. Variability with depth

The experimental and best-fit numerical concentrations for the GDP 15-m drifters and the subsurface Argo and RAFOS floats are presented in Fig. 6 (the corresponding scattered plots are available in supplemental Figs. S2 and S3). The diffusion coefficient is maximum in the upper 200 m (4630–4980 m^2 s^{-1}) and decreases with depth, with minimum values in the 1400–2000-m depth range (1080–1270 m^2 s^{-1}). A discrepant much smaller value occurs at 700–800 m (260 m^2 s^{-1}), but these data correspond largely to waters south of the Southern Boundary, where the flow is generally much weaker (supplemental Fig. S6).

b. Variability per frontal regions

The GDP and Argo programs provide sufficient drifting data to examine the spatial variability at 15 and 1000 m. Hence, we use the frontal systems (Fig. 1d)—Subtropical Front (STF), SAF, PF, SACCF, and SB—to separate the study area in five approximately zonal regions: STF to SAF, SAF to PF, PF to SACCF, SACCF to SB, and south of SB (Fig. 7). Each 10-day cycle is attributed to one single region.

The most dynamic regions of our study area are STF–SAF and SAF–PF. The STF–SAF region is characterized by the intense Malvinas Current and the mesoscalar features associated with the Brazil–Malvinas Confluence (Jullion et al. 2010; Mason et al. 2017; Artana et al. 2018; Orúe-Echevarría et al. 2019, 2021), and the SAF–PF region is distinguished by the intense currents associated with both frontal systems (Orsi et al. 1995; Naveira Garabato et al. 2003; Sokolov and Rintoul 2007; Olivé Abelló et al. 2021). The flow in PF–SACCF and SACCF–SB decreases in intensity (Naveira Garabato et al. 2003; Olivé Abelló et al. 2021) and the region south of the SB, which includes the Powell Basin in the Weddell Sea, displays even lower velocities (Yamazaki et al. 2021; Reeve et al. 2019; Vernet et al. 2019).

The 15-m diffusivities are very large in all five regions, with values in the 4000–5000 m^2 s^{-1} range, and only slightly less (3850 m^2 s^{-1}) in the domain south of SB, possibly reflecting the very intense winds in the whole area (Russell et al. 2006). At 1000 m, the range of diffusivities is consistent with the intensity of the zonal jets and eddies, with peak values in the STF–SAF (1640 m^2 s^{-1}) and SAF–PF (1820 m^2 s^{-1}) regions, and the minimum ones again south of the SB (530 m^2 s^{-1}).

5. Discussion

a. Limitations and advantages of the method

The ROD method has limitations and advantages, both conceptual and experimental. From a conceptual perspective, the method has several constraints. First, both the data analysis and the diffusion model assume that motions are radial, ignoring the vertical motions that a float may experience during one cycle. Free motions in the ocean (those that do not experience the restoring gravitational force) take place along isentropic (approximately isopycnal) tilted surfaces; hence, large subgrid motions during one single 10-day cycle could bring the float into neighboring vertical zones, with different

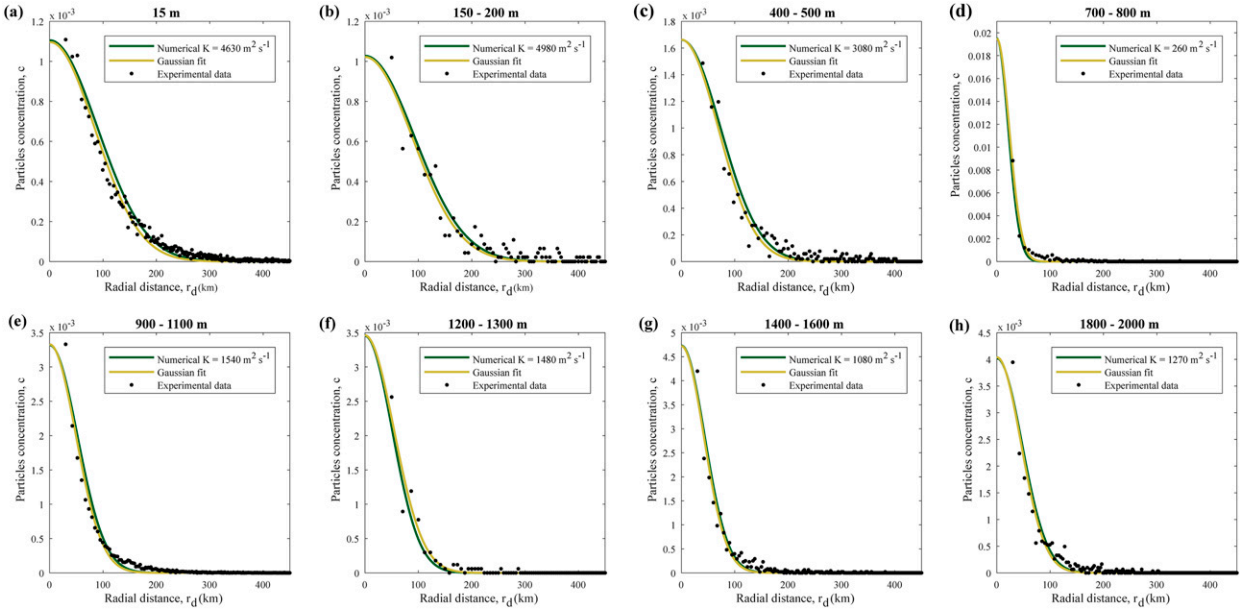

FIG. 6. Gaussian adjustment (light green line) to the experimental particle concentrations (black dots) and the best-adjusted numerical solution (dark green line) with the corresponding diffusion coefficient for each depth range as labeled. In all instances the correlation (R^2) between the experimental and numerical Gaussian curves, using data every 420 m, is greater than 0.95.

diffusive regimes; e.g., if a float experiences a displacement of 100 km across a frontal system with a 0.005 isopycnal slope then the depth change would be of 500 m. This indeed may be happening in some of our floats that drift close to frontal systems, but our data show that it is more an exception than a rule, with no substantial effect on the overall results (supplemental Fig. S1). In any case, it is possibly only a matter of thinking in terms of isopycnal rather than horizontal diffusivity, with diffusivity changes occurring with potential density rather than depth.

A second conceptual limitation of the ROD method is the assumption that the coefficient of diffusion K does not depend on the polar coordinate, which essentially means that turbulence is isotropic. This may not be so in the ocean because of topographic and/or dynamic constraints, e.g., differences in one order of magnitude (from 220 $m^2\ s^{-1}$ latitudinal to 1500 $m^2\ s^{-1}$ zonal) have been estimated in the deep South Atlantic because of the presence of alternating zonal jets (Herbei et al. 2008). In particular, for our study area, geophysical turbulence is likely influenced by the frontal systems, with a preferential alongfront (dominantly zonal) dispersive direction (Naveira Garabato et al. 2007; Roach et al. 2016). This shows up in the scattered plots (supplemental Figs. S2 and S3), which illustrate clouds of points (radial offsets) that are slightly elongated in certain directions. Obviously, the entire method could be modified by replacing the polar coordinates with a Cartesian coordinate system, where the major axis would be aligned with the front and the minor axis would be in the cross-frontal direction. The observations could be adjusted with a two-dimensional Gaussian surface and the diffusion equation would be solved in Cartesian coordinates, with different alongfront and cross-front diffusivities. This type of approximation could be important for studying large-scale meridional heat transport in regions such as the Southern Ocean.

The major conceptual and methodological advantage of the ROD method is precisely its simplicity, in accordance with its initial objective of providing model-suited horizontal diffusivity. As it is, the ROD method can be easily implemented, either with model reanalysis data or with forecast models. Actually, the ROD method was initially inspired by our desire to use a climatological daily output from GLORYS12v1 to explore the transfer of intermediate and mode Subantarctic waters all the way to the North Atlantic Ocean. Setting appropriate effective diffusivities is very important for daily velocity fields, as shown in this paper, but it is even more important for daily climatological velocity fields. Indeed, our preliminary results (not shown) evidence that the effective diffusivity for daily climatological velocity outputs has to be substantially greater than for actual daily velocity values.

From an experimental viewpoint, the ROD method is limited by the accuracy of the position fixings. In this regard, the use of a time interval of 10 days brings several advantages. First, water parcels traveling with typical speeds in the range of 0.05–0.5 m s^{-1} will travel distances between 43 and 430 km in 10 days. These trajectories will certainly not be straight but represent net displacements on the order of 10–100 km, long enough to easily adjust a Gaussian curve to the data points. Further, these displacements range from the submesoscale to the mesoscale, so they should allow assessing the effective diffusivity associated with the third phase of diffusion (Garrett 1983; Sundermeyer and Price 1998). Finally, these distances are much larger than the accuracy in the drifters' positioning (1–100 m for the GDP and about 1 km for RAFOS and Argo floats), granting further confidence to the good performance and robustness of the method.

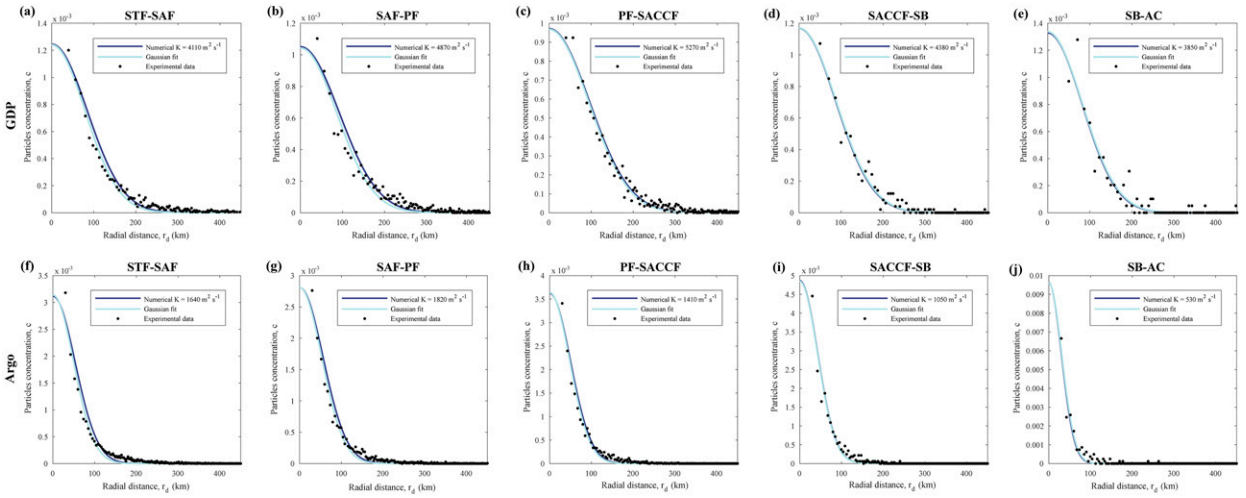

FIG. 7. Gaussian adjustment (light blue line) to the experimental particle concentrations (black dots) and the best-adjusted numerical solution (dark blue line) with the corresponding diffusion coefficient for each region as labeled; the acronyms are Subtropical Front (STF), Subantarctic Front (SAF), Polar Front (PF), Southern Antarctic Circumpolar Current Front (SACCF), Southern Boundary (SB), and Antarctic continent (AC). (a)–(e) GDP data at 15-m depth and (f)–(j) Argo data in the 900–1100-m depth range. In all instances the correlation (R^2) between the experimental and numerical Gaussian curves, using data every 420 m, is greater than 0.95.

The one-dimensional radial diffusion equation appears as a sensible, simple yet realistic, option to simulate subgrid motions that are not resolved in numerical circulation models. It has also been used by other authors to explore the stirring properties of either floats or numerical particles through the temporal changes in the probability density functions (LaCasce 2010; Graff et al. 2015; Balwada et al. 2021). We may further explore the validity of this approximation by comparing the coefficients provided by the method with the expression that relates the diffusivity K with the variance of the radial offsets σ^2 during some relatively long time scale τ, long enough for the effective eddy diffusivity to develop (LaCasce et al. 2014; Roach et al. 2016):

$$K = \frac{\sigma^2}{2\tau}. \tag{2}$$

We have used Eq. (2) for the eight depth ranges where we have applied the ROD method (Fig. 6), with σ^2 as obtained from the Gaussian distribution adjusted to the experimental particle concentrations and $\tau = 10$ days (Fig. 8). A scattered plot of the K data shows very good agreement between the experimental $\sigma^2/2\tau$ and radial-diffusion values, with a slope of 0.92 and a correlation coefficient of 0.99, hence granting further confidence to the ROD approach.

b. *Comparison with other observations for the study area*

We end up comparing our results for the study area with horizontal diffusivity estimates from other studies. A summary of our estimates for K as a function of depth and region is shown in Fig. 9. In general, the horizontal diffusivity decreases with depth from values close to 5000 m^2 s^{-1} in the near-surface waters to values about 1100–1300 m^2 s^{-1} between 1500 and 2000 m (Fig. 9a). The single exception is the mean value at 750 m (700–800-m depth range), which shows a discrepant low value of 260 m^2 s^{-1}. This dissimilarity could be related to a real decrease in the subgrid variability at these depths but it seems more likely that it responds to the fact that a substantial fraction of the data at these depths corresponds to Argo floats drifting south of the Southern Boundary, even within the Weddell Sea with the presence of substantial ice coverage (supplemental Fig. S6). Therefore, it seems plausible that this low value responds to different dominant dynamic processes (Yamazaki et al. 2021; Reeve et al. 2019; Vernet et al. 2019).

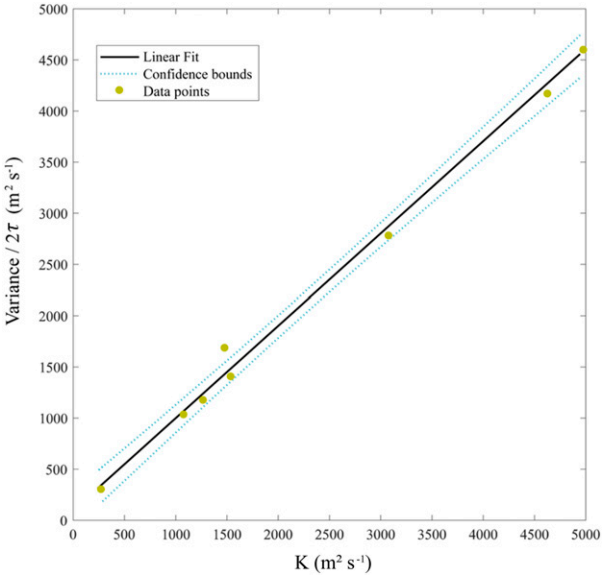

FIG. 8. Scattered plot of the experimental $\sigma^2/2\tau$ values as a function of the K values obtained through the ROD method. The linear regression is shown together with the 0.95 confidence bounds.

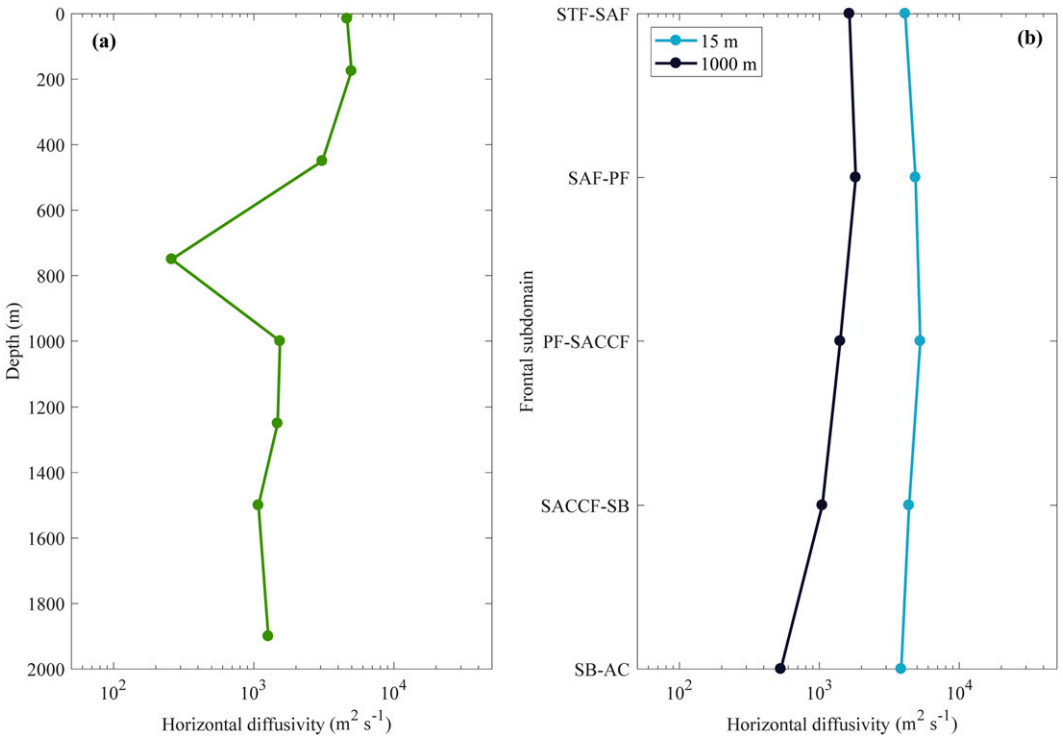

FIG. 9. (a) Vertical distribution of the horizontal diffusion coefficients. (b) Horizontal variability of these coefficients at 15-m depth (light blue dots) and in the 900–1100-m depth range (dark blue dots) for the five frontal regions (Fig. 1d). The acronyms are Subtropical Front (STF), Subantarctic Front (SAF), Polar Front (PF), Southern Antarctic Circumpolar Current Front (SACCF), Southern Boundary (SB), and Antarctic continent (AC). Notice that the diffusion coefficients are plotted on a logarithmic scale.

The 15-m horizontal diffusion coefficients are fairly similar in all regions, probably reflecting that the surface layer is directly influenced by the intense westerly winds in the entire study area (Russell et al. 2006). In contrast, the 900–1100-m values do have a latitudinal pattern, with maximum values linked to the intense Subtropical, Subantarctic, and Polar Fronts (1640–1820 m^2 s^{-1}), halfway values between the Polar Front and the Southern Boundary (1050–1410 m^2 s^{-1}), and minimum values south of the Southern Boundary (530 m^2 s^{-1}). Notice that the fast jet and high variability associated with the Polar Front takes place north of its surface location [see Fig. 4 in Naveira Garabato et al. (2011) and Figs. 7 and 12 in Olivé Abelló et al. (2021)], within the SAF–PF region.

There is an extraordinary range of horizontal diffusion values reported in the literature. As explained in the introduction, this is because the spreading of properties depends on the spatio-temporal scales that we allow the dispersive processes to take place, with the last phase—which acts from the submesoscale to the mesoscale—producing the effective diffusion. Cole et al. (2015) and Roach et al. (2018) have provided global maps of this effective horizontal diffusivity.

Using 3° × 3° data from both the Argo program and a global numerical circulation model, Cole et al. (2015) found values roughly ranging between 200 and 20 000 m^2 s^{-1} at the base of the winter mixed layer, with the largest values in the western boundary currents and the equatorial jets. Zonally averaged values for each ocean basin, show peak surface values of about 10 000 m^2 s^{-1} that decrease down to 100–1000 m^2 s^{-1} near 2000-m depth. Roach et al. (2018) used GDP and Argo float data gridded at 1° × 1° to calculate the asymptotic eddy diffusivity, which they estimated takes place at time scales of order 10 days near the sea surface and 100 days at 1000 m; in these calculations, the effect of the mean-flow in suppressing the eddy-related diffusion was considered (Ferrari and Nikurashin 2010). They estimated the global mean eddy diffusivity to be 2637 ± 311 m^2 s^{-1} at the sea surface and 543 ± 155 m^2 s^{-1} at 1000 m, with maximum surface values in the western boundary currents and the equatorial jets, and maximum 1000-m values in the western boundary currents and along the Antarctic Circumpolar Current (ACC).

Several studies have explored the intensity of horizontal mixing in the Southern Ocean (Table 1), of special relevance because of its key role in the global overturning circulation. Sallée et al. (2011) used sea surface height data (1/3° daily) to estimate characteristic surface diffusivities ranging between 1500 m^2 s^{-1} near the center of the ACC and 3000 m^2 s^{-1} in its northern flank. Naveira Garabato et al. (2011) used 22 hydrographic sections combined with sea surface height data (1/3° weekly) and found that K is intensified in the interfrontal regions, with values of about 2000 m^2 s^{-1}, and is suppressed in the jet cores, with values of about 200 m^2 s^{-1}, although with exceptions in some segments. These values are fairly

TABLE 1. Comparison of our horizontal diffusivity estimates with results from other authors.

Author	Depth	Region	Diffusivity values K (m^2 s^{-1})
Naveira Garabato et al. (2007)	200–2000 m	Scotia Sea	1840 ± 440
Sallée et al. (2011)	Sea surface	North and center of the ACC	1500–3000
Naveira Garabato et al. (2011)	Upper 1000 m	Interfrontal ACC	200–2000
Tulloch et al. (2014)	1500 m	Drake Passage	1200 ± 500
Cole et al. (2015)	Winter mixed layer	Global	200–20 000
Roach et al. (2016)	1000 m	ACC	300–2500
Roach et al. (2018)	Sea surface	Global mean	2637 ± 311
	1000 m		543 ± 155
Roach et al. (2018)	1000 m	Scotia Sea	1019 ± 158
		Southern Ocean	658 ± 125
This study—ROD method	15 m	Western South Atlantic	3850–5270
	1000 m		530–1820

uniform in the upper 1000 m of the water column, decreasing with depth in the underlying layers. Roach et al. (2016) explored the size of eddy diffusivity at 1000 m using several datasets: numerical at 1/6° and 5-day resolution, sea surface height at 1/3° and daily resolution, together with the 10-day Argo and daily RAFOS data. The datasets were analyzed with different methods, leading to several types of cross-flow effective diffusivities (named meridional, cross contour, and cross stream) that take 10–50 days to reach asymptotic values between about 300 and 2500 m^2 s^{-1}. In a posterior study, Roach et al. (2018) calculated the Southern Ocean 1000-m effective diffusivity to be 658 ± 125 m^2 s^{-1}. Tulloch et al. (2014), from a tracer spreading experiment upstream of the Drake Passage, estimated a diffusivity of 1200 ± 500 m^2 s^{-1} at 1500 m.

In the Scotia Sea, tracking natural helium injected from hydrothermal vents near Drake Passage into the ACC, Naveira Garabato et al. (2007) estimated a regional K average of 1840 ± 440 m^2 s^{-1} for the entire Upper Circumpolar Deep Waters (UCDW), spanning depths from a few hundred meters down to about 2000 m. Also for the Scotia Sea, Roach et al. (2018) obtained a 1000-m effective diffusivity value of 1019 ± 158 m^2 s^{-1}.

All the above studies show that the horizontal diffusivity decreases with depth, with values of several thousand square meters per second near the sea surface and between several hundred and a few thousand square meters per second in the intermediate and deep layers. The large range of values is possibly not surprising considering the variety of datasets (with very different spatiotemporal resolution) and methodologies employed. In any case, it is encouraging to see that the horizontal diffusivities obtained with the simple ROD method are consistent with the previously reported numbers.

6. Final remarks

The description of horizontal geophysical diffusivity remains a major conceptual and experimental challenge. As oceanographers, we often wonder what horizontal diffusion coefficient is most appropriate for a certain study, whether it be a climatological basinwide balance or a coastal application of a numerical circulation model. Motivated by this dilemma, we have developed the radial offset by diffusion (ROD) method, as a simple yet robust approach that combines drifter and numerical trajectories to provide a first-order estimate of horizontal diffusivity K. Testing the ROD method in the Subantarctic and Antarctic waters of the southwestern Atlantic Ocean has shown that it does provide realistic coefficients of horizontal diffusivity.

The ROD method is model dependent, whether it be a numerical prediction or any directly or indirectly observed velocity field, in the sense that it provides K values that are only appropriate for that specific application. Using these coefficients with other models of similar spatiotemporal resolution is likely adequate but should be done with caution. Nevertheless, because of its simplicity, it could be easily implemented for other applications. For example, we could easily increase the time interval of the studied trajectories in order to explore the asymptotic character of effective diffusivity, particularly in deep waters [as extensively discussed by Roach et al. (2018)].

The ROD method also allows reducing the size of the domain under study, an important feature in order to investigate regional variations in mixing. For example, Naveira Garabato et al. (2011) argue that eddy mixing in the Southern Ocean is suppressed in frontal regions, where eddies propagate much slower than the mean flow. This leads to the counterintuitive idea that frontal jets, with increased eddy kinetic energy, may actually have relatively small cross-stream horizontal diffusion. These authors further propose the existence of leaky sectors in jets, where cross-frontal mixing would not be inhibited. The ROD method appears as a potentially useful tool to explore this type of variability, e.g., focusing on frontal systems and regions with rough topography. In particular, we have found that the region between the Polar Front and the Subantarctic Front displays the maximum K values. These two fronts are by far the most intense in the Scotia Sea (Naveira Garabato et al. 2011; Olivé Abelló et al. 2021) so it is plausible that the turbulent eddies generated in both neighboring frontal systems could propagate into this relatively sluggish interfrontal region, where eddy-induced mixing would not be suppressed.

The ROD method is a simple and cost-effective tool for assessing ocean lateral diffusivity, a key parameter for many applications, from the dispersion of properties in numerical circulation models to inverse-type regional balances. Thanks to the continuous increase in drifter data and the expanded availability of high-resolution numerical models and reanalysis, the ROD method could be applied basinwide to quantify

how mixing affects large-scale circulation, or used locally to investigate the relevance of different submesoscale and mesoscale processes in the distribution of water properties.

Acknowledgments. This work has been funded by the Spanish Government through project SAGA (Ministerio de Ciencia, Innovación y Universidades, Reference RTI2018-100844-B-C33). AOA is grateful to the FPU program, funded by the Spanish Government (Ministerio de Educación, Cultura y Deporte, Reference FPU17/03796). We happily acknowledge the International Argo Program, the contributing national programs that are part of the Global Ocean Observing System, and the Coriolis website that collects and distribute the data. We sincerely thank the Copernicus Marine Environment Monitoring Service for making available the GLORYS12v1 numerical reanalysis and the National Oceanic and Atmospheric Administration for distributing the GDP and RAFOS datasets. We are also very grateful to Chad Greene for making available the Southern Ocean Database. Further, we want to acknowledge the Ocean Parcels team who developed the code and made it open source to the entire oceanographic community. Finally, we thank our two anonymous reviewers and our editor, Gilberto Javier Fochesatto, for their encouragement and for providing a number of very useful suggestions. This article is a publication of the Unidad Océano y Clima of the Universidad de Las Palmas de Gran Canaria, an R+D+I CSIC-associate unit. The authors also recognize the institutional support of the Spanish Government through the Severo Ochoa Center of Excellence accreditation (CEX2019-000928-S).

Data availability statement. No new datasets were generated during this study. All datasets are available through the Copernicus Marine Environment Monitoring Service (CMEMS; http://marine.copernicus.eu), the International Argo Program of the Global Ocean Observing System (http://www.argo.net/), the Global Drifter Program of the National Oceanic and Atmospheric Administration (https://globalocean.noaa.gov/Research/Global-Drifter-Program), and the Atlantic Oceanographic and Meteorological Laboratory of the National Oceanic and Atmospheric Administration (https://www.aoml.noaa.gov/phod/float_traj/data.php). The ROD method developed in this article is fully reproducible. The analysis of the data has been done with MATLAB (version 2017a) and Python (version 3.6.10), and the Ocean Parcels project code (version 2.2.1) is available at https://oceanparcels.org/. The ROD method configurations, data, and scripts are freely available in Olivé Abelló et al. (2023), and they can also be accessed at https://git.csic.es/a-simple-method-for-estimating-horizontal-diffusivity/rod_method.

REFERENCES

Abernathey, R. P., and J. Marshall, 2013: Global surface eddy diffusivities derived from satellite altimetry. *J. Geophys. Res. Oceans*, **118**, 901–916, https://doi.org/10.1002/jgrc.20066.

Argo, 2000: Argo float data and metadata from Global Data Assembly Centre (Argo GDAC). SEANOE, accessed 19 August 2022, https://doi.org/10.17882/42182.

Artana, C., and Coauthors, 2018: Fronts of the Malvinas Current system: Surface and subsurface expressions revealed by satellite altimetry, Argo floats, and Mercator operational model outputs. *J. Geophys. Res. Oceans*, **123**, 5261–5285, https://doi.org/10.1029/2018JC013887.

Babiano, A., C. Basdevant, P. Le Roy, and R. Sadourny, 1990: Relative dispersion in two-dimensional turbulence. *J. Fluid Mech.*, **214**, 535–557, https://doi.org/10.1017/S0022112090000258.

Balwada, D., K. G. Speer, J. H. LaCasce, W. B. Owens, J. Marshall, and R. Ferrari, 2016: Circulation and stirring in the southeast Pacific Ocean and the Scotia Sea sectors of the Antarctic Circumpolar Current. *J. Phys. Oceanogr.*, **46**, 2005–2027, https://doi.org/10.1175/JPO-D-15-0207.1.

——, J. H. LaCasce, K. G. Speer, and R. Ferrari, 2021: Relative dispersion in the Antarctic Circumpolar Current. *J. Phys. Oceanogr.*, **51**, 553–574, https://doi.org/10.1175/JPO-D-19-0243.1.

Boland, E. J. D., E. Shuckburgh, P. H. Haynes, J. R. Ledwell, M.-J. Messias, and A. J. Watson, 2015: Estimating a submesoscale diffusivity using a roughness measure applied to a tracer release experiment in the Southern Ocean. *J. Phys. Oceanogr.*, **45**, 1610–1631, https://doi.org/10.1175/JPO-D-14-0047.1.

Chiswell, S. M., 2013: Lagrangian time scales and eddy diffusivity at 1000 m compared to the surface in the South Pacific and Indian Oceans. *J. Phys. Oceanogr.*, **43**, 2718–2732, https://doi.org/10.1175/JPO-D-13-044.1.

CLS, 2011: Argos user's manual. CLS, http://www.argos-system.org/manual/.

Cole, S. T., C. Wortham, E. Kunze, and W. B. Owens, 2015: Eddy stirring and horizontal diffusivity from Argo float observations: Geographic and depth variability. *Geophys. Res. Lett.*, **42**, 3989–3997, https://doi.org/10.1002/2015GL063827.

Davis, R. E., 1987: Modeling eddy transport of passive tracers. *J. Mar. Res.*, **45**, 635–666, https://doi.org/10.1357/002224087788326803.

——, 1991a: Lagrangian ocean studies. *Annu. Rev. Fluid Mech.*, **23**, 43–64, https://doi.org/10.1146/annurev.fl.23.010191.000355.

——, 1991b: Observing the general circulation with floats. *Deep-Sea Res.*, **38A**, S531–S571, https://doi.org/10.1016/S0198-0149(12)80023-9.

De Dominicis, M., G. Leuzzi, P. Monti, N. Pinardi, and P.-M. Poulain, 2012: Eddy diffusivity derived from drifter data for dispersion model applications. *Ocean Dyn.*, **62**, 1381–1398, https://doi.org/10.1007/s10236-012-0564-2.

Delandmeter, P., and E. Van Sebille, 2019: The Parcels v2.0 Lagrangian framework: New field interpolation schemes. *Geosci. Model Dev.*, **12**, 3571–3584, https://doi.org/10.5194/gmd-12-3571-2019.

Deng, Z.-C., Y.-C. Hon, and L. Yang, 2014: An optimal control method for nonlinear inverse diffusion coefficient problem. *J. Optim. Theory Appl.*, **160**, 890–910, https://doi.org/10.1007/s10957-013-0302-z.

Döös, K., V. Rupolo, and L. Brodeau, 2011: Dispersion of surface drifters and model-simulated trajectories. *Ocean Modell.*, **39**, 301–310, https://doi.org/10.1016/j.ocemod.2011.05.005.

Elipot, S., R. Lumpkin, R. C. Perez, J. M. Lilly, J. J. Early, and A. M. Sykulski, 2016: A global surface drifter dataset at hourly resolution. *J. Geophys. Res. Oceans*, **121**, 2937–2966, https://doi.org/10.1002/2016JC011716.

Ferrari, R., and M. Nikurashin, 2010: Suppression of eddy diffusivity across jets in the Southern Ocean. *J. Phys. Oceanogr.*, **40**, 1501–1519, https://doi.org/10.1175/2010JPO4278.1.

Garrett, C., 1983: On the initial streakiness of a dispersing tracer in two- and three-dimensional turbulence. *Dyn. Atmos. Oceans*, **7**, 265–277, https://doi.org/10.1016/0377-0265(83)90008-8.

Garric, G., and Coauthors, 2017: Performance and quality assessment of the global ocean eddy-permitting physical reanalysis GLORYS2V4. *Proc. Eighth EuroGOOS Int. Conf.*, Bergen, Norway, EuroGOOS, 215–222.

Gent, P. R., and J. C. McWilliams, 1990: Isopycnal mixing in ocean circulation models. *J. Phys. Oceanogr.*, **20**, 150–155, https://doi.org/10.1175/1520-0485(1990)020<0150:IMIOCM>2.0.CO;2.

Graff, L. S., S. Guttu, and J. H. LaCasce, 2015: Relative dispersion in the atmosphere from reanalysis winds. *J. Atmos. Sci.*, **72**, 2769–2785, https://doi.org/10.1175/JAS-D-14-0225.1.

Herbei, R., I. W. McKeague, and K. G. Speer, 2008: Gyres and jets: Inversion of tracer data for ocean circulation structure. *J. Phys. Oceanogr.*, **38**, 1180–1202, https://doi.org/10.1175/2007JPO3835.1.

Jullion, L., K. J. Heywood, A. C. Naveira Garabato, and D. P. Stevens, 2010: Circulation and water mass modification in the Brazil–Malvinas Confluence. *J. Phys. Oceanogr.*, **40**, 845–864, https://doi.org/10.1175/2009JPO4174.1.

LaCasce, J. H., 2008: Statistics from Lagrangian observations. *Prog. Oceanogr.*, **77**, 1–29, https://doi.org/10.1016/j.pocean.2008.02.002.

——, 2010: Relative displacement probability distribution functions from balloons and drifters. *J. Mar. Res.*, **68**, 433–457, https://doi.org/10.1357/002224010794657155.

——, R. Ferrari, J. Marshall, R. Tulloch, D. Balwada, and K. Speer, 2014: Float-derived isopycnal diffusivities in the DIMES experiment. *J. Phys. Oceanogr.*, **44**, 764–780, https://doi.org/10.1175/JPO-D-13-0175.1.

Lange, M., and E. van Sebille, 2017: Parcels v0.9: Prototyping a Lagrangian ocean analysis framework for the petascale age. *Geosci. Model Dev.*, **10**, 4175–4186, https://doi.org/10.5194/gmd-10-4175-2017.

Lebedev, K. V., H. Yoshinari, N. A. Maximenko, and P. W. Hacker, 2007: YoMaHa'07: Velocity data assessed from trajectories of Argo floats at parking level and at the sea surface. IPRC Tech. Note 4, 16 pp., http://apdrc.soest.hawaii.edu/projects/yomaha/yomaha07/YoMaHa070612.pdf.

Ledwell, J. R., A. J. Watson, and C. S. Law, 1998: Mixing of a tracer in the pycnocline. *J. Geophys. Res.*, **103**, 21 499–21 529, https://doi.org/10.1029/98JC01738.

Lellouche, J.-M., and Coauthors, 2021: The Copernicus global 1/12° oceanic and sea ice GLORYS12 reanalysis. *Front. Earth Sci.*, **9**, 698876, https://doi.org/10.3389/feart.2021.698876.

Mason, E., A. Pascual, P. Gaube, S. Ruiz, J. L. Pelegrí, and A. Delepoulle, 2017: Subregional characterization of mesoscale eddies across the Brazil-Malvinas Confluence. *J. Geophys. Res. Oceans*, **122**, 3329–3357, https://doi.org/10.1002/2016JC012611.

Mercator Ocean, 2018: Product sheet: Native grid product–reanalysis–global ocean–PHY–1/12°. Mercator Ocean International Doc., 2 pp., https://www.mercator-ocean.eu/wp-content/uploads/products_pdf/MOI_GLORYS12.pdf.

Mignac, D., D. Ferreira, and K. Haines, 2018: South Atlantic meridional transports from NEMO based simulations and reanalyses. *Ocean Sci.*, **14**, 53–68, https://doi.org/10.5194/os-14-53-2018.

Nakamura, N., 1996: Two-dimensional mixing, edge formation, and permeability diagnosed in an area coordinate. *J. Atmos. Sci.*, **53**, 1524–1537, https://doi.org/10.1175/1520-0469(1996)053<1524:TDMEFA>2.0.CO;2.

Naveira Garabato, A. C., D. P. Stevens, and K. J. Heywood, 2003: Water mass conversion, fluxes and mixing in the Scotia Sea diagnosed by an inverse model. *J. Phys. Oceanogr.*, **33**, 2565–2587, https://doi.org/10.1175/1520-0485(2003)033<2565:WMCFAM>2.0.CO;2.

——, ——, A. J. Watson, and W. Roether, 2007: Short-circuiting of the overturning circulation in the Antarctic Circumpolar Current. *Nature*, **447**, 194–197, https://doi.org/10.1038/nature05832.

——, R. Ferrari, and K. L. Polzin, 2011: Eddy stirring in the Southern Ocean. *J. Geophys. Res.*, **116**, C09019, https://doi.org/10.1029/2010JC006818.

Olivé Abelló, A., J. L. Pelegrí, F. J. Machín, and I. Vallès-Casanova, 2021: The transfer of Antarctic Circumpolar waters to the western South Atlantic Ocean. *J. Geophys. Res. Oceans*, **126**, e2020JC017025, https://doi.org/10.1029/2020JC017025.

——, ——, and ——, 2023: The radial offset by diffusion (ROD) method (v1.0.0). Zenodo, accessed 30 March 2023, https://doi.org/10.5281/zenodo.7449421.

Ollitrault, M., M. Lankhorst, D. Fratantoni, P. Richardson, and W. Zenk, 2006: Zonal intermediate currents in the equatorial Atlantic Ocean. *Geophys. Res. Lett.*, **33**, L05605, https://doi.org/10.1029/2005GL025368.

Orsi, A. H., T. Whitworth III, and W. D. Nowlin Jr., 1995: On the meridional extent and fronts of the Antarctic Circumpolar Current. *Deep-Sea Res. I*, **42**, 641–673, https://doi.org/10.1016/0967-0637(95)00021-W.

Orúe-Echevarría, D., J. L. Pelegrí, F. Machín, A. Hernández-Guerra, and M. Emelianov, 2019: Inverse modeling the Brazil-Malvinas Confluence. *J. Geophys. Res. Oceans*, **124**, 527–554, https://doi.org/10.1029/2018JC014733.

——, and Coauthors, 2021: A view of the Brazil-Malvinas Confluence, March 2015. *Deep-Sea Res. I*, **172**, 103533, https://doi.org/10.1016/j.dsr.2021.103533.

Peña-Izquierdo, J., E. van Sebille, J. L. Pelegrí, J. Sprintall, E. Mason, P. J. Llanillo, and F. Machín, 2015: Water mass pathways to the North Atlantic oxygen minimum zone. *J. Geophys. Res. Oceans*, **120**, 3350–3372, https://doi.org/10.1002/2014JC010557.

Reeve, K. A., O. Boebel, V. Strass, T. Kanzow, and R. Gerdes, 2019: Horizontal circulation and volume transports in the Weddell Gyre derived from Argo float data. *Prog. Oceanogr.*, **175**, 263–283, https://doi.org/10.1016/j.pocean.2019.04.006.

Roach, C. J., D. Balwada, and K. Speer, 2016: Horizontal mixing in the Southern Ocean from Argo float trajectories. *J. Geophys. Res. Oceans*, **121**, 5570–5586, https://doi.org/10.1002/2015JC011440.

Roach, L. A., C. Horvat, S. M. Dean, and C. M. Bitz, 2018: An emergent sea ice floe size distribution in a global coupled ocean-sea ice model. *J. Geophys. Res. Oceans*, **123**, 4322–4337, https://doi.org/10.1029/2017JC013692.

Roberts, M., and D. Marshall, 1998: Do we require adiabatic dissipation schemes in eddy-resolving ocean models? *J. Phys. Oceanogr.*, **28**, 2050–2063, https://doi.org/10.1175/1520-0485(1998)028<2050:DWRADS>2.0.CO;2.

Roemmich, D., and Coauthors, 2022: The Argo program. *Partnerships in Marine Research: Case Studies, Lessons Learned, and Policy Implications*, G. Auad and F. K. Wiese, Eds., Science of Sustainable Systems, Elsevier, 53–69.

Rosell-Fieschi, M., J. L. Pelegrí, and J. Gourrion, 2015: Zonal jets in the equatorial Atlantic Ocean. *Prog. Oceanogr.*, **130**, 1–18, https://doi.org/10.1016/j.pocean.2014.08.008.

Rossby, T., D. Dorson, and J. Fontaine, 1986: The RAFOS system. *J. Atmos. Oceanic Technol.*, **3**, 672–679, https://doi.org/10.1175/1520-0426(1986)003<0672:TRS>2.0.CO;2.

Rühs, S., V. Zhurbas, I. M. Koszalka, J. V. Durgadoo, and A. Biastoch, 2018: Eddy diffusivity estimates from Lagrangian trajectories simulated with ocean models and surface drifter

data—A case study for the greater Agulhas system. *J. Phys. Oceanogr.*, **48**, 175–196, https://doi.org/10.1175/JPO-D-17-0048.1.

Russell, J. L., K. W. Dixon, A. Gnanadesikan, R. J. Stouffer, and J. R. Toggweiler, 2006: The Southern Hemisphere westerlies in a warming world: Propping open the door to the deep ocean. *J. Climate*, **19**, 6382–6390, https://doi.org/10.1175/JCLI3984.1.

Sallée, J., K. Speer, and S. R. Rintoul, 2011: Mean-flow and topographic control on surface eddy-mixing in the Southern Ocean. *J. Mar. Res.*, **69**, 753–777, https://doi.org/10.1357/002224011799849408.

Skeel, R. D., and M. Berzins, 1990: A method for the spatial discretization of parabolic equations in one space variable. *SIAM J. Sci. Stat. Comput.*, **11** (1), 1–32, https://doi.org/10.1137/0911001.

Sokolov, S., and S. R. Rintoul, 2007: Multiple jets of the Antarctic Circumpolar Current south of Australia. *J. Phys. Oceanogr.*, **37**, 1394–1412, https://doi.org/10.1175/JPO3111.1.

Sundermeyer, M. A., and J. F. Price, 1998: Lateral mixing and the North Atlantic Tracer Release Experiment: Observations and numerical simulations of Lagrangian particles and a passive tracer. *J. Geophys. Res.*, **103**, 21 481–21 497, https://doi.org/10.1029/98JC01999.

Tulloch, R., and Coauthors, 2014: Direct estimate of lateral eddy diffusivity upstream of Drake Passage. *J. Phys. Oceanogr.*, **44**, 2593–2616, https://doi.org/10.1175/JPO-D-13-0120.1.

Vallès-Casanova, I., E. Fraile-Nuez, M. Martín-Rey, E. van Sebille, A. Cabré, A. Olivé-Abelló, and J. L. Pelegrí, 2022: Water mass transports and pathways in the North Brazil–equatorial undercurrent retroflection. *J. Geophys. Res. Oceans*, **127**, e2021JC018150, https://doi.org/10.1029/2021JC018150.

Vernet, M., and Coauthors, 2019: The Weddell Gyre, Southern Ocean: Present knowledge and future challenges. *Rev. Geophys.*, **57**, 623–708, https://doi.org/10.1029/2018RG000604.

Yamazaki, K., S. Aoki, K. Katsumata, D. Hirano, and Y. Nakayama, 2021: Multidecadal poleward shift of the southern boundary of the Antarctic Circumpolar Current off East Antarctica. *Sci. Adv.*, **7**, eabf8755, https://doi.org/10.1126/sciadv.abf8755.

Zhurbas, V., and I. S. Oh, 2003: Lateral diffusivity and Lagrangian scales in the Pacific Ocean as derived from drifter data. *J. Geophys. Res.*, **108**, 3141, https://doi.org/10.1029/2002JC001596.

——, D. A. Lyzhkov, and N. P. Kuzmina, 2014: Estimates of the lateral eddy diffusivity in the Indian Ocean as derived from drifter data. *Oceanology*, **54**, 281–288, https://doi.org/10.1134/S0001437014030163.

Zika, J. D., T. J. McDougall, and B. M. Sloyan, 2010: A tracer-contour inverse method for estimating ocean circulation and mixing. *J. Phys. Oceanogr.*, **40**, 26–47, https://doi.org/10.1175/2009JPO4208.1.